TU Delft

Delft University of Technology

Simulating big mechanically-active culture systems (BigMACS) using paired biomechanics-histology FEA modelling to derive mechanobiology design relationships

Schoenborn, Sabrina; Yuan, Mingyang; Fell, Cody A.; Liu, Chuanhai; Fletcher, David F.; Priola, Selene; Chan, Hon Fai; Woodruff, Mia; Li, Zhiyong; Toh, Yi Chin

DOI
10.1088/1758-5090/adcd9f

Publication date
2025

Document Version
Final published version

Published in
Biofabrication

Citation (APA)
Schoenborn, S., Yuan, M., Fell, C. A., Liu, C., Fletcher, D. F., Priola, S., Chan, H. F., Woodruff, M., Li, Z., Toh, Y. C., & Allenby, M. C. (2025). Simulating big mechanically-active culture systems (BigMACS) using paired biomechanics-histology FEA modelling to derive mechanobiology design relationships. *Biofabrication*, *17*(3), Article 035006. https://doi.org/10.1088/1758-5090/adcd9f

Important note
To cite this publication, please use the final published version (if applicable).
Please check the document version above.

Copyright
Other than for strictly personal use, it is not permitted to download, forward or distribute the text or part of it, without the consent of the author(s) and/or copyright holder(s), unless the work is under an open content license such as Creative Commons.

Takedown policy
Please contact us and provide details if you believe this document breaches copyrights.
We will remove access to the work immediately and investigate your claim.

This work is downloaded from Delft University of Technology.
For technical reasons the number of authors shown on this cover page is limited to a maximum of 10.

International Society for Biofabrication
PURPOSE-LED PUBLISHING™

PAPER • **OPEN ACCESS**

Simulating big mechanically-active culture systems (BigMACS) using paired biomechanics-histology FEA modelling to derive mechanobiology design relationships

To cite this article: Sabrina Schoenborn *et al* 2025 *Biofabrication* **17** 035006

View the article online for updates and enhancements.

You may also like

- 3D bioprinting technology for modeling vascular diseases and its application
Ju-El Kim, Gun-Jae Jeong, Young Min Yoo et al.
- Biomedical implication of microfluidics in disease diagnosis and therapeutics: from fabrication to prognosis
Shivani Yadav, Manish Dwivedi, Sukriti Singh et al.
- Efficient one-step immobilization of DNA probes on 1DZnO nanoplatforms targeting a low-mutation region of SARS-CoV-2
Shirlley Martínez Tolibia, Rafael A Salinas, Cesar Millán-Pacheco et al.

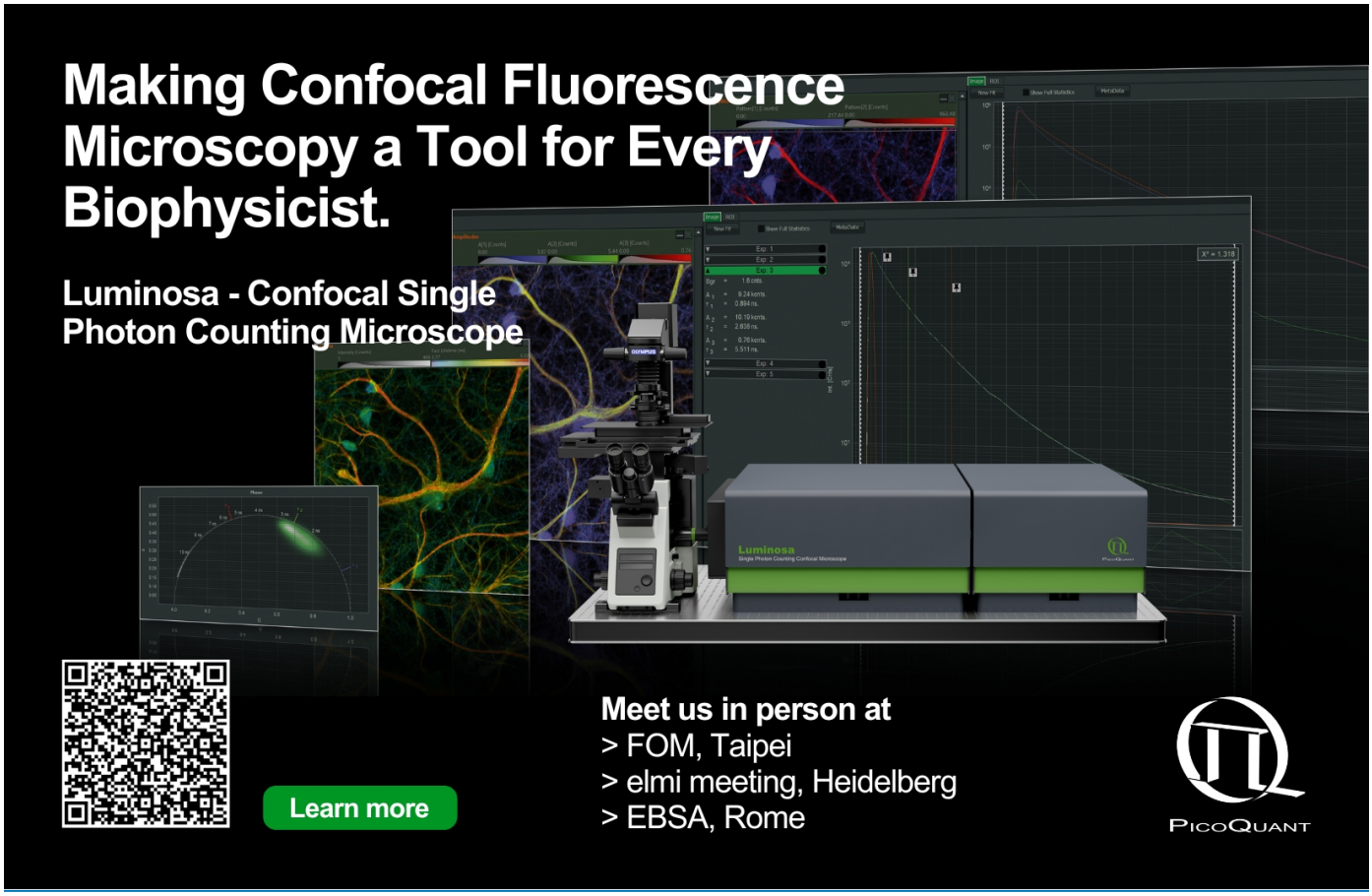

This content was downloaded from IP address 145.90.33.240 on 12/05/2025 at 08:31

Biofabrication

PAPER

Simulating big mechanically-active culture systems (BigMACS) using paired biomechanics-histology FEA modelling to derive mechanobiology design relationships

Sabrina Schoenborn[1,2], Mingyang Yuan[1,2], Cody A Fell[2], Chuanhai Liu[3,4], David F Fletcher[5], Selene Priola[6], Hon Fai Chan[3,4], Mia Woodruff[2], Zhiyong Li[2], Yi-Chin Toh[2] and Mark C Allenby[1,2,*]

[1] BioMimetic Systems Engineering (BMSE) Lab, School of Chemical Engineering, University of Queensland (UQ), St Lucia QLD 4072, Australia
[2] Centre for Biomedical Technologies, School of Mechanical, Medical, and Process Engineering, Queensland University of Technology, Kelvin Grove, Queensland, Australia
[3] Key Laboratory for Regenerative Medicine of the Ministry of Education of China, School of Biomedical Sciences, Faculty of Medicine; Institute for Tissue Engineering and Regenerative Medicine, The Chinese University of Hong Kong, Shatin, Hong Kong Special Administrative Region of China, People's Republic of China
[4] Center for Neuromusculoskeletal Restorative Medicine, Hong Kong Special Administrative Region of China, People's Republic of China
[5] School of Chemical and Biomolecular Engineering, University of Sydney, Darlington, NSW 2006, Australia
[6] Department of Biomechanical Engineering, Faculty of Mechanical Engineering, Delft University of Technology, Delft, The Netherlands
* Author to whom any correspondence should be addressed.

E-mail: m.allenby@uq.edu.au, sabrina@schoenborn.tech, mingyang.yuan@hdr.qut.edu.au, Cody.Fell@Rice.edu, liuchuanhai@link.cuhk.edu.hk, david.fletcher@sydney.edu.au, S.Pirola@tudelft.nl, honfaichan@cuhk.edu.hk, mia.woodruff@qut.edu.au, zhiyong.li@qut.edu.au and yichin.toh@qut.edu.au

OPEN ACCESS

RECEIVED
24 February 2025

REVISED
9 April 2025

ACCEPTED FOR PUBLICATION
16 April 2025

PUBLISHED
28 April 2025

Original content from this work may be used under the terms of the Creative Commons Attribution 4.0 licence.

Any further distribution of this work must maintain attribution to the author(s) and the title of the work, journal citation and DOI.

Keywords: computational simulation, biomechanics, mechanobiology, computer vision, bioimage analysis

Supplementary material for this article is available online

Abstract

Big mechanically-active culture systems (BigMACS) are promising to stimulate, control, and pattern cell and tissue behaviours with less soluble factor requirements. However, it remains challenging to predict if and how distributed mechanical forces impact single-cell behaviours to pattern tissue. In this study, we introduce a tissue-scale finite element analysis framework able to correlate sub-cellular quantitative histology with centimetre-scale biomechanics. Our framework is relevant to diverse BigMACS, including media perfusion, tensile-stress, magnetic, and pneumatic tissue culture platforms. We apply our framework to understand how the design and operation of a multi-axial soft robotic bioreactor can spatially control mesenchymal stem cell (MSC) proliferation, orientation, differentiation to smooth muscle, and extracellular vascular matrix deposition. We find MSC proliferation and matrix deposition to positively correlate with mechanical stimulation but cannot be locally patterned by soft robot mechanical stimulation within a centimetre scale tissue. In contrast, local stress distribution was able to locally pattern MSC orientation and differentiation to smooth muscle phenotypes, where MSCs aligned perpendicular to principal stress direction and expressed increased α-SMA with increasing 3D Von Mises Stresses from 0 to 15 kPa. Altogether, our new biomechanical-histological simulation framework is a promising technique to derive the future mechanical design equations to control cell behaviours and engineer patterned tissue.

1. Introduction

The engineering of lab-grown cell and tissue products depends, in part, on the mechanical environment that cells are exposed to [1]. There have been decades of research into the negative effects of mechanical stress; how the stiffness of different cell culture substrates alters the potency or differentiation of cells [2, 3], or how media perfusion imparts shear stresses that can impair cell health during culture [4, 5]. More recently, big mechanically-active culture systems (BigMACS) have been engineered to improve

© 2025 The Author(s). Published by IOP Publishing Ltd

lab-grown cell and tissue product biomanufacturing [6, 7]. BigMACS include perfusion bioreactors to up-scale manufacturing [8], tensile stress bioreactors to improve myogenic differentiation [9], and soft robotic bioreactors whose on-demand flexion can enable non-invasive cell harvest [10]. BigMACS platforms are promising to enhance cell and tissue biomanufacturing but, to date, remain limited by inconsistent outcomes and an incomplete understanding of how their mechanical forces influence cell behaviours.

The impact of MACS mechanics on cell behaviour is typically evaluated by finite element analysis (FEA), with computational modelling correlated to tissue histology [11–13]. A major shortcoming of this approach is that FEA approaches are often based on continuum mechanics theory focussed on tissue-scale analysis. These existing FEA approaches do not capture how local mechanical forces influence single-cell behaviours [14]. Cellular mechanotransduction depends on each cell's local stresses (single-cell mechano-transduction), as well as the mechanics and actions that neighbouring cells experience (in paracrine mechano-transduction) [15]. Furthermore, MACS platforms often contain mechanical or structural artefacts at the microscale (such as microroughness caused during fabrication processes) [16], too miniscule to capture at the millimetre-to-centimetre tissue scale, which can greatly affect the local mechanics that a cell senses [17]. If we want to know how much mechanical stress to apply, to a specific region of our culture, at a specific time in culture, to control cell behaviour and to pattern lab-grown tissue, we must create new single-cell-scale mechanical models which capture the single cell microscale, as well as tissue mesoscale relevant to mechanotransduction.

In 2022, our group published details of a soft robotic bioreactor for mesenchymal stem cell (MSC) culture [18]. We designed our soft robotic bioreactor to model the radial and angular multi-axial mechanical forces found within the human femoropopliteal artery while standing, walking, and crouching in normal and diseased cases. We found increasing mechanical forces with values similar to those in our body's normal femoropopliteal artery led to increased MSC proliferation, alignment, and smooth muscle cell (SMC) differentiation in the absence of soluble differentiation factors. Although limited to bulk tissue analysis, local MSC behaviours appeared to be patterned by the quantity and angle of the mechanical forces we applied in our soft robotic bioreactor, as also observed by other studies using pneumatic and soft robotic MACS platforms with distributed mechanical forces [10, 19–22]. If we could define a predictive relationship between mechanical forces and patterned tissue generation, we could engineer more realistic and functional lab-grown cell and tissue products.

In this paper, we develop a biomechanics-histology framework for the simulation of BigMACSs as applied to our prior soft robotic femoropopliteal artery bioreactor. Our approach utilises a FEA mesh of an extremely high resolution (10^{6-7} nodes cm^{-2}), 100–1000-fold more dense than a confluent cell monolayer, necessary to investigate the effect of mechanical forces on single-cells on a 3D printed scaffold. This FEA mesh resolution is essential as microrough surfaces are often unavoidable in BigMACS and 3D printed platforms, and microrough surfaces play important roles in single-cell mechano-transduction [23]. Scaling our single-cell-scale simulations to tens of thousands of cells within centimetres of mechanically-stimulated tissue, we quantitatively understand whether and how local mechanical stress influence cell density, orientation, differentiation (MSCs to SMCs), and matrix deposition (collagen type-4). Our models indicate several of these mechanically-directed cell behaviours appear to occur or stop once a threshold stress magnitude is reached.

This paper proposes a single-cell biomechanics-histology predictive modelling framework which seeks to uncover fundamental design equations in mechanobiology at scales relevant to the nascent cell and tissue biomanufacturing industry. We believe these new approaches could have a broad impact across cell and tissue types and small to big mechanically active culture systems (BigMACS).

2. Materials and methods

2.1. Fabricating the BigMACS soft robotic femoropopliteal artery bioreactor

Soft robotic bioreactors were engineered within a previous study [18] to model the complex multi-axial mechanics of our knee's femoropopliteal artery, where up to 80% of peripheral cardiovascular diseases are found [24, 25]. Femoropopliteal artery mechanics include cyclical radial distension (RD) during every cardiac cycle (13%/0.67 Hz) and angular flexions (AFs) while walking (153°/0.5 Hz). To simultaneously control radial and angular distension, a three-chambered soft robot was designed, consisting of a central air channel that could be pressurised for a RD, and left and right air channels connected to pneumatic networks, a common soft robotics approach to enable for left and right angular distension, as visualised in table 1.

To fabricate the soft robotic bioreactor, two-part soft robotic bioreactor moulds were printed from 3D Tuff resin (Monocure 3D, Sydney, Australia) using a digital light projection printer (DLP, Creality LD-002R, Shenzhen, China), washed, and further cured. Platsil OO-20 silicone was poured into the top and bottom moulds and placed onto a hotplate at 60 °C for at least 2 h until solidified. Two-part Platsil OO-20 silicone casts were then adhered to one another with a thin layer of Platsil OO-20 silicone and placed back onto the hotplate for an additional 2 h.

Table 1. BigMACS mechanical stimulation conditions. Four mechanical conditions were compared with three or four biological replicates each. Conditions included a static control, angular flexion, radial distension, and angular flexion and radial dissension combined. Bending angle and frequency replicated the angle and frequency of mechanical stimulation in the human femoropopliteal artery while walking. Adapted from [18]. © IOP Publishing Ltd. All rights reserved.

Conditioning group	Bending angle/-frequency (Hz)	Percent radial distension/frequency (Hz)	Deformation schematic
Static control	0°/0.0 Hz	0%/0.0 Hz	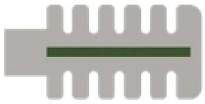
Angular flexion	153°/0.5 Hz	0%/0.0 Hz	
Radial distension	0°/0.0 Hz	13%/0.67 Hz	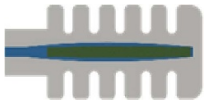
Angular + radial combined	153°/0.5 Hz	13%/0.67 Hz	

A rectangular recess (30.5 × 2 mm) in the soft robotic BigMACS bioreactor was coated with 10 μg ml^{-1} fibronectin and then seeded at 3 × 10^4 TeloASC52 MSCs/cm^2 (American Type Culture Collection) and expanded for 3 d until confluent. Then, soft robotic BigMACS bioreactors were pressurised by a custom rack-and-pinion syringe pump to undergo static, angular, radial, or angular and radial stress cycles every 1–2 s for 24 h (roughly 50 000 cycles), as described in table 1.

MSCs were cultured in MSC basal medium (#PCS-500-030; ATCC) mixed with MSC growth kit (#PCS-500-040; ATCC) and 200 μg ml^{-1} G418 antibiotic (Thermo Fisher, Seventeen Mile Rocks, Australia). Cells were cultured in a humidified incubator at 37 °C and 5% CO2 for cell expansion, viability, and conditioning experiments. Cultures were then fixed with 4% paraformaldehyde (PFA), stained with rabbit anti-human collagen type 4 (col-IV), goat anti-human α-smooth muscle actin (α-SMA), phalloidin to stain cytoskeletal actin, and 4′,6-diamidino-2-phenylindole (DAPI) to stain cell nuclei. Soft robotic BigMACS were then imaged by a Nikon A1R confocal microscope (Tokyo, Japan).

2.2. BigMACS FEA ANSYS simulation

Due to the large deformation of the soft-robot particularly during bending, a hyperelastic third-order Ogden model was chosen to describe the PlatSil® Gel-OO20 (Polytek) silicone material model [26, 27]:

Table 2. Third-order Ogden model parameters of PlatSil soft robot model. Incompressibility parameters d_i, material constants α_i, material constants μ_i.

μ_i [MPa]	α_1 [−]	d_i [MPa^{-1}]
$\mu_1 = 1.4736 \times 10^{-2}$	$\alpha_1 = 3.41576$	$d_1 = 3.2587$
$\mu_2 = 6.6703 \times 10^{-5}$	$\alpha_2 = 7.0679$	$d_2 = 0$
$\mu_3 = 4.5381 \times 10^{-4}$	$\alpha_3 = -3.3659$	$d_3 = 0$

$$W = \sum_{i=1}^{3} \frac{\mu_i}{\alpha_i} \left(\overline{\lambda}_1^{\alpha_i} + \overline{\lambda}_2^{\alpha_i} + \overline{\lambda}_3^{\alpha_i} - 3 \right) + \sum_{k=1}^{3} \frac{1}{d_k} (J-1)^{2k}$$

where W is the strain energy potential, $\overline{\lambda}_1$, $\overline{\lambda}_2$, $\overline{\lambda}_3$ are reduced principal stretches defined as $\overline{\lambda}_i = J^{-\frac{1}{3}} \lambda_i$, where λ_i is the principal stretch of the left Cauchy–Green tensor. J is the determinant of the elastic deformation gradient, and μ_i, α_i and d_k are material constants.

The initial shear modulus μ is defined as follows:

$$\mu = \tfrac{1}{2} \sum_{i=1}^{3} \alpha_i \mu_i.$$

The Ogden model parameters were determined using the Ansys hyperelastic curve fitting function on uniaxial tensile data generated with the manufactured dog bone samples and biaxial and compressibility data from literature [28], with initial bulk modulus $K = 2/d_1$, as summarised in table 2.

All three actuation groups of the original study were simulated by FEA: RD conditioning with 13% stretch cyclically at 0.67 Hz, AF conditioning with a 153° angle of actuation cyclically at 0.5 Hz and a combined angular-radial (AR) conditioning. The cyclic actuation pressure provided by a syringe pump in the original study was modelled as a pressure boundary condition acting on the internal pneumatic channels and the resulting deformation of the soft robot model was analysed to ensure it matched the deformation of the experimental devices. The model was set up as 3D, quadratic and incompressible. Rigid body motion was prevented by applying a fixed support to the base area of the model, which was constrained by a rigid casing connecting it to the syringe pump in the experimental setup. The effect of gravity was included as -9806.6 mm s^{-2} in the z-dimension. A timestep was considered as converged when the force convergence value and the displacement convergence value were both below a residual target of 10^{-4}. The model was run on the University of Queensland's Bunya supercomputer [29] as a transient analysis using the sparse direct solver with a time-step size of 10 ms ensuring solver convergence and satisfying the timestep sensitivity analysis.

The maximum element size for the meshing of the cell culture area was 10 μm corresponding to a node density of 50 620 per mm^2. While mesh convergence was achieved for larger element sizes, this value was chosen to facilitate a more detailed comparison between the histology imaging data and the numerical data since the average cell size of the MSCs utilised in this study was 50 μm. However, during imaging, the presence of microgrooves resulting from stereolithography (SLA) 3D printing layer lines were noted at an average periodicity of 105 μm tip-to-tip (figure 1(A)). In the cell culture study, a small effect on cellular morphology and alignment was observed, which was not significant compared with the effect of the actuation. To facilitate a comparison of the local stress–strain profiles of both the ideal CAD geometry and the manufactured micro-grooved geometry with the histology imaging data, the original CAD model was modified to include these layer lines across the cell culture area of the model (figure 1(A)).

This Ansys FEA simulation calculated all normal stresses $(\sigma_x, \sigma_y, \sigma_z)$ and shear stresses $(\tau_{xy}, \tau_{xz}, \tau_{yz})$ for millions of simulated nodes. To estimate stress magnitude, we used 3D Von Mises stress as an Ansys output and also calculated 3D Von Mises Stress [30] for verification from our FEA simulation's node output as:

$$\sigma_v = \sqrt{\frac{\left(\sigma_{xx}-\sigma_{yy}\right)^2+\left(\sigma_{yy}-\sigma_{zz}\right)^2+\left(\sigma_{zz}-\sigma_{xx}\right)^2+6\left(\tau_{xy}^2+\tau_{yz}^2+\tau_{zx}^2\right)}{2}}.$$

To estimate principal stress direction, we calculated 2D Von Mises Stress by setting the final dimension $\sigma_i = 0$. We also calculated angles of deviance from a principal stress tensor (Mohr's Circle) [31, 32]. In the XY-plane, the Mohr's Circle calculation is written as:

$$MA_{xy} = \frac{180}{2\pi}\sin^{-1}\left(-\tau_{xy}/\sqrt{\tau_{xy}^2+\left(\sigma_x-\frac{\sigma_x+\sigma_y}{2}\right)^2}\right).$$

In the main figures of this paper, we focussed on 3D Von Mises Stress and angle on XY Mohr's circle, but we have included all 2D Von Mises Stress and angle on XZ, YZ Mohr's circle plots in the supplemental figure.

2.3. BigMACS quantitative histology image analysis and statistics

The centre region of the soft robotic BigMACS culture recess was imaged by confocal microscopy by stitching together eight 3D image tiles (4 × 2 tilescan; roughly 20 mm^2 of cell culture space) using NIS-Elements (Nikon). Col-IV, α-SMA, actin, and DAPI stains were detected with ImageJ's particle analysis plugin, and actin cytoskeletal orientation was measured with ImageJ's OrientationJ plugin [33]. These measurements were exported as comma-separated value spreadsheets with each row listing the location, intensity, and orientation of each Col-IV, α-SMA, actin, and DAPI stain, with 5000–100 000 rows per stain per soft robotic bioreactor. These spreadsheets were imported into python to correlate each stain's local density (stain/cm^2) and orientation with the local 3D Von Mises Stress and XY Mohr's Angle, through a third order polynomial regression (Python's polyfit) as presented alongside 95% confidence intervals in figures 4 and 5. Measurement replicates calculated for the polynomial regression confidence intervals were considered as each individual stain in the image (with 5000–100 000 stains detected per image); it is important to note that only one biological and one image replicate were compared per soft robotic bioreactor condition.

Local stain density (stain/cm^2) was calculated for each stain by counting the number of stains within a 3D radius (e.g. 50 μm), projected to 2D by averaging the neighbour count for x and y pairs, and dividing by its circular area (7850 μm^2).

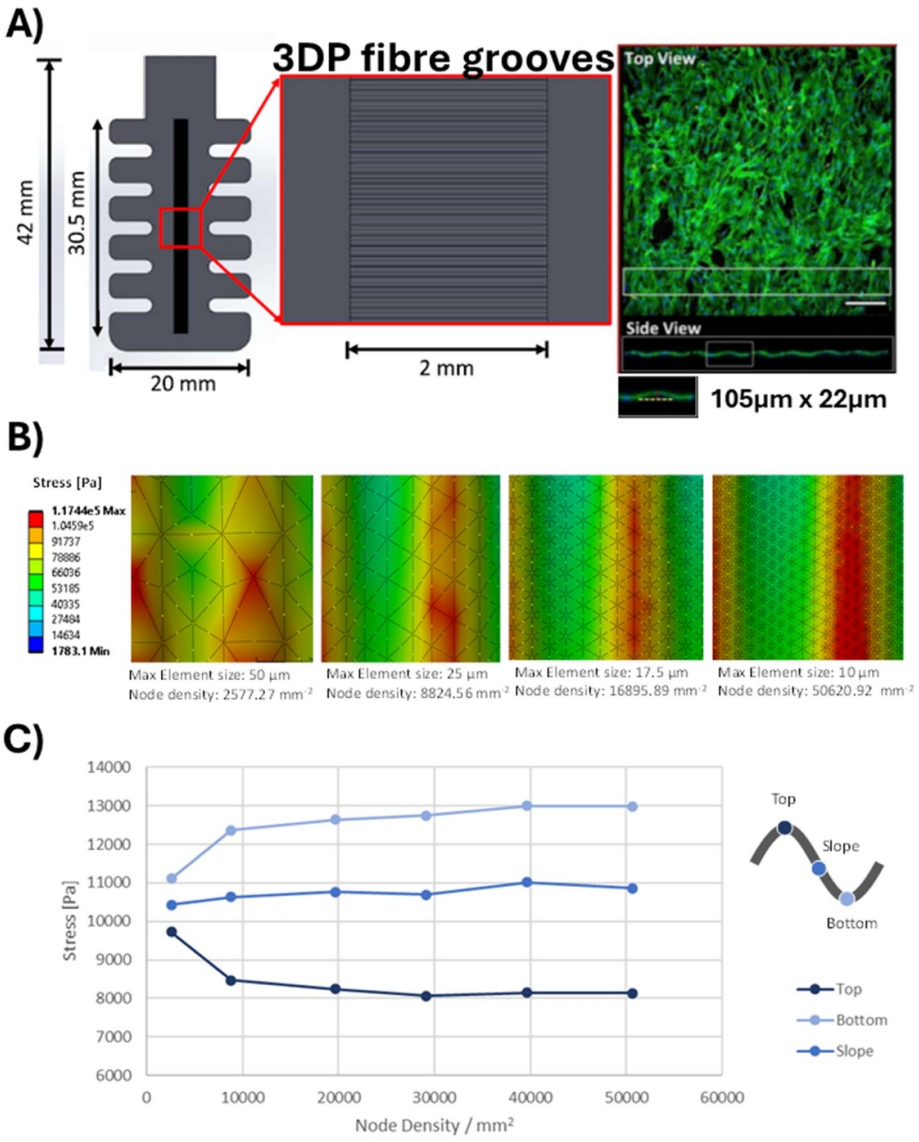

Figure 1. BigMACS geometry and FEA mesh sensitivity analysis. (A) Illustration of the BigMACS platform, showing the presence of microgrooves in the cell culture chamber, with confocal imagery of the 22 µm tall groove height. (B) Mechanical stress results of micro-grooved BigMACS under radial distension with various FEA mesh resolutions, showing inconsistent stress profiles below 10 000 mesh nodes per mm^2. (D) Sensitivity of FEA mesh node density on Von Mises stress at top, bottom, and mid-point slope areas. Subfigure A is a modified version of supplemental data from [18]. Adapted from [18]. © IOP Publishing Ltd. All rights reserved.

However, this approach creates edge effects when measuring local density for stains on the edge of the image, where part of the circle's area is outside the imaging space, an image analysis challenge previously recognised [34]. To overcome this edge effect, we mirrored the distribution of cells on the opposite side of each of four 2D imaging edges (left, right, top, bottom). As the imaging edges were sometimes irregular (due to artefacts) we preformed this mirroring exercise for many discrete steps along each edge, outlined in supplemental figure S1.

3. Results

3.1. Simulating BigMACS requires micro-resolved FEA due to 3D printing micro-artefacts

A mesh sensitivity analysis on the grooved soft robotic model indicates that the computational cost of resolving microgrooves in the model is considerable compared with resolving to a cellular level. Since the microgrooves generated via SLA printing (105 μm) are approximately twice the size of an average MSC (50 μm), the microgrooves cannot be sufficiently modelled using a mesh of this size and

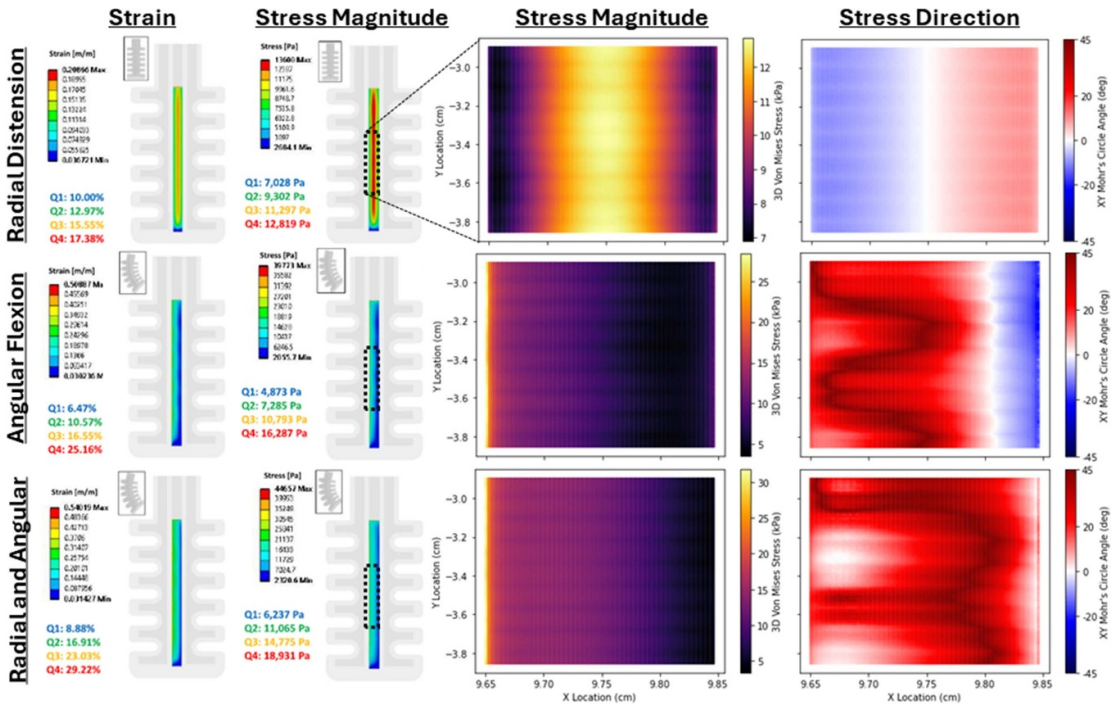

Figure 2. Biomechanics simulations of BigMACS. Full-scale strain and stress-magnitude simulations of BigMACS under radial distension, angular flexion, and radial and angular distension. (Right) Stress magnitude (3D Von Mises Stress) and stress direction (*XY* Mohr's Angle) of a cell culture region imaged by confocal microscopy.

local stress gradients between the top and bottom of grooves are not resolved (figures 1(B) and (C)). An element size of 25 μm (25% the size of the groove) allows for the resolution of a distinct stress gradient along the groves but it requires an element size of approximately 10 μm or 10% of the size of the microgroove to reach a mesh convergence target of below 2% resulting in an increase in node number of over 1960% for the micro-grooved cell culture region compared with a maximum element size of 50 μm.

The results obtained with a maximum element size of 10 μm demonstrates the significant effect of microgrooves on local stress values, with stresses at the top and bottom of grooves fluctuating 20%–30% around the respective average stress on a flat surface. Where microgrooves need to be numerically resolved, the required node density in our study increased by a factor of 20 from a mesh-independent smooth model to a mesh-independent micro-grooved model, indicating that the elimination of microgrooves for *in-vitro*/in-silico coupled models is highly beneficial with regards to computational cost. Smooth BigMACS simulations required 100-fold fewer nodes to achieve mesh convergence (10^4 instead of 10^6 nodes/cm^2), in-line with existing approaches. A comparison of micro-grooved versus smoothed soft robotic bioreactor Von Mises stress normal and shear stresses and Mohr's stress angles are in supplemental figures S2–S7, while a comparison of micro-grooved and smoothed histological images can be found in our prior publication's supplemental data [18]. The effect of micro-grooves were neglected as their effect appeared to be less significant than the effect of BigMACS actuation.

3.2. BigMACS exhibit highly heterogenous mechanical stress gradients

The stress simulations illustrated the highly heterogeneous mechanical stresses applied to the soft robotic BigMACS cell culture area (figure 2). BigMACS undergoing RD exhibited a bulge in their cell culture area, turning the concave recess into a convex bulge, and applying maximum and average 3D Von Mises Stress of 14 kPa and 10 kPa, concentrated at the centre of the cell culture recess. RD bioreactors exhibited symmetric XY Mohr's Angle to the left and right of the culture recess, with XY Mohr's Angles from −30 to +30 degrees.

The BigMACS undergoing AF exhibited a much higher maximum but lower average 3D Von Mises stress than RD (40 kPa, 8.5 kPa), concentrated on the outer arc of the bending culture recess (left side), which dissipated quickly when moving across the culture recess to the inner arc (right side). The AF bioreactor's *XY* Mohr's Angle was greatly affected by the presence of microgrooves every 105 μm but also by

the pneumatic chambers spaced every 500 μm on the sides of the soft robot. During AF, the pneumatic chambers along the inner arc resist compression and create a stress oriented in the opposite direction on the right-hand side of the culture recess.

The BigMACS undergoing AF exhibited a much higher maximum but lower average 3D Von Mises stress than RD (40 kPa, 8.5 kPa), concentrated on the outer arc of the bending culture recess (left side), which dissipated quickly when moving across the culture recess to the inner arc (right side). The AF bioreactor's *XY* Mohr's Angle was greatly affected by the presence of microgrooves every 105 μm but also by the pneumatic chambers spaced every 500 μm on the sides of the soft robot. During AF, the pneumatic chambers along the inner arc resist compression and create a stress oriented in the opposite direction on the right-hand side of the culture recess.

When combining RD with AF, the maximum and average 3D Von Mises Stress are somewhat higher than AF and RD, respectively (50 kPa, 13 kPa), and the soft robot's compressed pneumatic chambers offered less resistance against AF, exhibited by a consistently positive *XY* Mohr's Angle. These simulations illustrate the complex microscale stress gradients impacting 3D printed and soft robotic BigMACS, due to microrough artefacts and pneumatic chambers ubiquitous to their production and designs, able to create significant impact at the cell scale.

3.3. BigMACS conditioning alters cell behaviours at bulk and local scale

After four days of growth, or three days of growth and one day of mechanical conditioning, all four soft robot mechanical conditions exhibited confluent cell coverage across their culture recess (figure 3(A)). Interestingly, all types of mechanical conditioning caused this confluent layer to become much more packed with cells, as quantitative histology analyses indicated that average nuclear density is five-fold higher for all mechanical conditioning regimes in comparison to the static control (figure 3(B)). Nuclear density appeared to not be locally correlated with microscale stress magnitude, except for the highest 3D Von Mises Stresses from 15 to 20 kPa (figure 4). The principal stress direction did not appear to correlate correlation to nuclear density. However, an AF *XY* Mohr's stress angle of $-5°$, where pneumatic channels along the soft robot's inner arc began to push back against AF (figure 3), appear to correlate with a higher difference in nuclear density (figure 5).

Cell orientation, measured as cytoskeletal protein actin orientation, was randomly aligned for static soft robot bioreactors both on the microscale and across the full image (figure 3). In contrast, mechanically-conditioned versus static BigMACS all expressed a larger number of brighter, longer, actin stains whose bulk orientation was increasingly aligned in a parallel direction to the major stress angle, especially for bioreactors with greater mechanical stress. Cell orientation for mechanically-conditioned BigMACS was consistent for the y -axis but varied along the x -axis, similar to how mechanical forces varied along x but not y. Interestingly, cell orientation appeared to be correlated with moderate stress magnitude (figure 4) and principal stress direction but only for radial BigMACS (figure 5). Cell orientation within radial and angular conditioned BigMACS responded to changes of low-magnitude mechanical stress (5–10 kPa), though cell orientation on radial and angular combined BigMACS changed for stress magnitudes above 20 kPa (figure 4). Cell orientation was inversely correlated to *XY* Mohr's angle for radial BigMACS, indicating that cells aligned perpendicular to principal stress direction (figure 5).

Smooth muscle differentiation occurs as a consequence of MSC mechanical conditioning, even in the absence of media-supplemented soluble myogenic factors. Smooth muscle differentiation of MSCs is phenotypically detected by an upregulation in alpha smooth muscle actin (α-SMA). We identified all α-SMA stains in confocal images which fluoresced brighter than their respective isotype controls, and then calculated the local density of α-SMA around each α-SMA stain. While negligible α-SMA was detected in static BigMACS, 10-to-20 greater α-SMA was found in all three mechanically conditioned BigMACS (figure 3). Mechanical stress magnitude was positively correlated with α-SMA stain density at lower 3D Von Mises Stress range (0–12 kPa) for all mechanically conditioned BigMACS, and then negatively correlated at higher 3D Von Mises Stresses (15–25 kPa; figure 4). This is in line with prior work suggesting super-physiological stress might shift cells to focus on survival or quiescence instead of smooth muscle differentiation [35, 36]. Expression of α-SMA in RD BigMACS was most intense near *XY* Mohr's stress angles of 0°; however, this is likely because it is where mechanical stress magnitude was greatest in RD. Similar trends were not found between α-SMA and principal stress direction for other mechanical BigMACS conditions (figure 5).

Matrix deposition of vascular collagen type 4 (Col-IV) from MSCs or SMCs, found in the basal lamina of arteries, is enhanced under mechanical stimulation [37]. Just as in the case of α-SMA, we identified all Col-IV stains in confocal images which fluoresced brighter than their respective isotype controls and then calculated the local density of

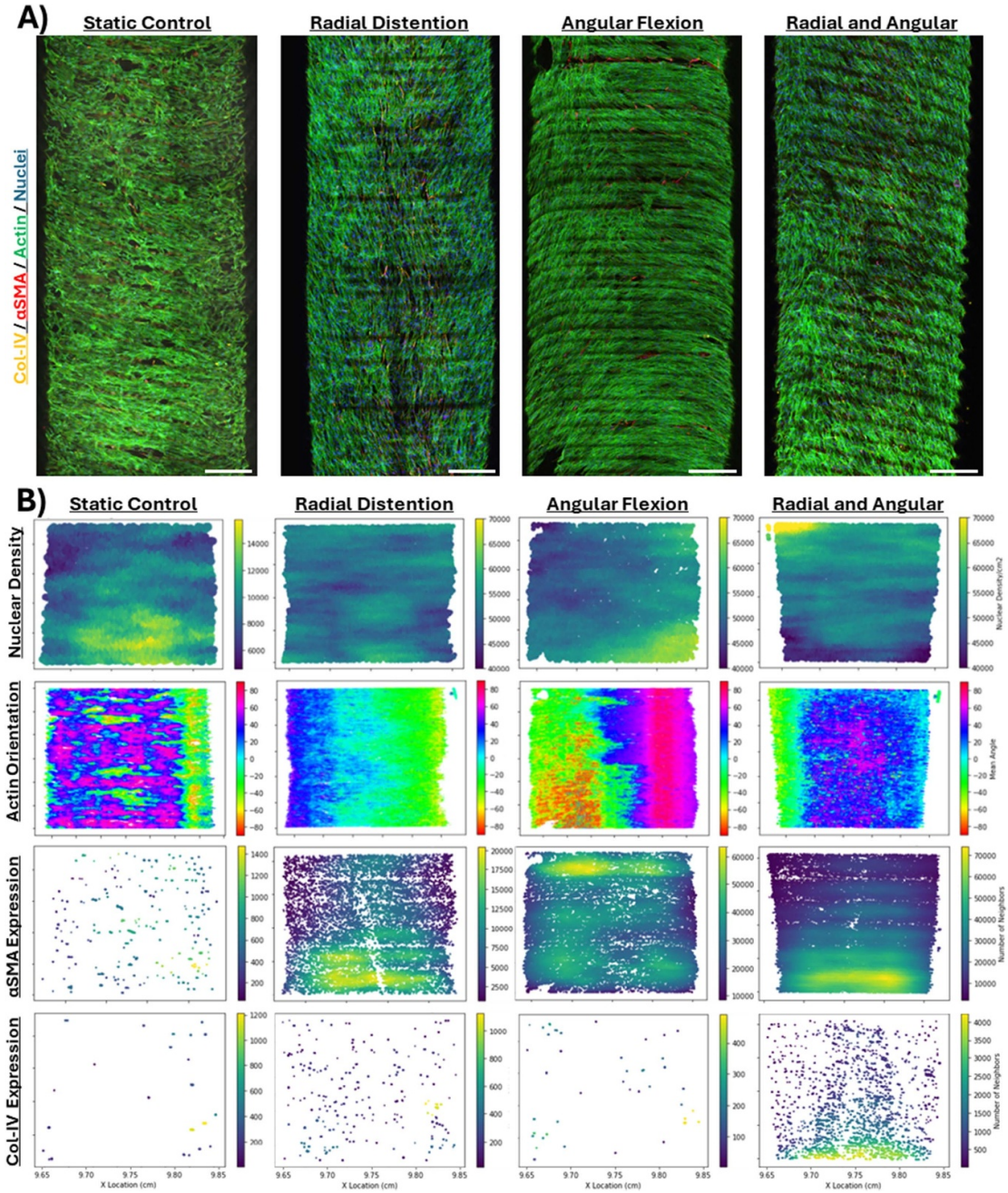

Figure 3. Quantitative histology of BigMACS conditioning. (A) MSCs were cultured in soft robotic bioreactors for four days in static (left), or for three days in static and one day in radial, angular, or radial and angular mechanical conditioning (right) and imaged by 4 × 2 tiled 3D confocal microscopy. Scale bars are 0.05 cm. (B) Computational histology analyses of the nuclear density, actin orientation, α-SMA stain density, and Col-IV stain density of the four BigMACS conditions (note that heatmap scales for the static control condition are several-fold lower than mechanically-active conditions).

Col-IV around each Col-IV stain. Col-IV was negligibly expressed in static BigMACS, more expressed in radial or angular conditioned BigMACS, and significantly more expressed in combined radial and angular BigMACS. No local Col-IV deposition trends were identified for radial or angular conditioning. For BigMACS with combined radial and angular conditioning, more Col-IV was deposited in the centre of the BigMACS, where there was an intermediate stress magnitude and positive principal stress direction (most BigMACS exhibited positive angles). While Col-IV was only deposited by MSCs in BigMACS conditioned with the highest stress magnitudes, this deposition seemed to occur across the whole culture chamber, and did not localise in regions of higher mechanical stress.

4. Discussion

Big mechanically active culture systems (BigMACS) have been applied in tissue engineering for more than two decades, with early and well-referenced examples including Altman *et al* [38]). BigMACS are of increasing importance in tissue engineering and regenerative

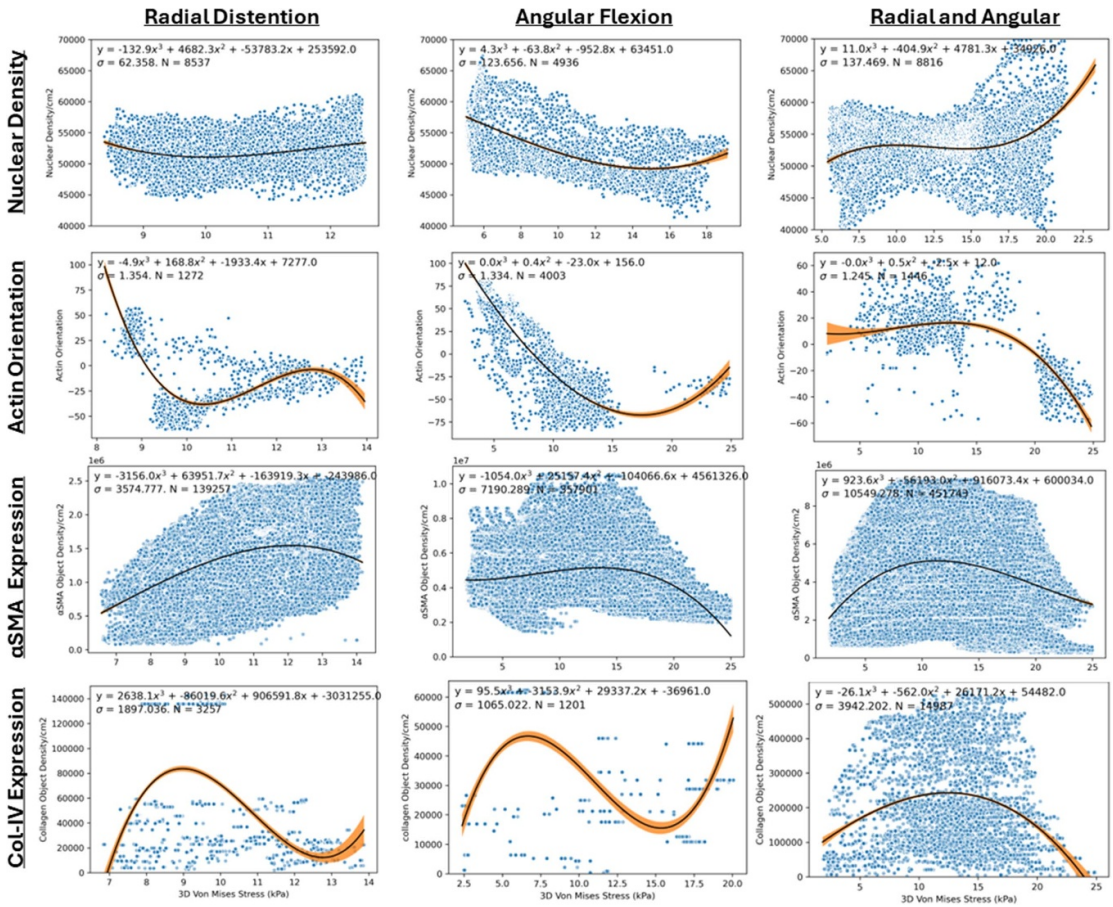

Figure 4. Impact of 3D Von Mises stress on BigMACS cell behaviours. Scatterplots of 3D Von Mises stress (kPa; *x*-axis) versus nuclear (DAPI stain) density, α-SMA stain density, and Col-IV stain density per cm^2 or average actin orientation, as calculated in a 50 μm radius around each detected stain. Third-order polynomials were fitted to the imaging data with 95% confidence intervals calculated. Regression statistical replicates were calculated as the number of stains detected per image (1201–451 749) and not imaging, experimental, or biological replicates.

medicine. These BigMACS apply dynamic mechanical forces which reproduce our body's natural fluid flow, locomotion, or flexion to model regeneration or disease, to distribute nutrients or growth factors for higher density cell growth, to trigger the continuous release of cell or cell-based products throughout culture (such as extracellular vesicles) [39–42], and, in this application, to promote stem cell proliferation or differentiation in the absence of exogenous factors.

In table 3, we summarise prior BigMACS which have been used in human MSC (hMSC) cultures. Most BigMACS apply uniaxial tensile strain to a thin cell culture substate, typically a (coated) silicone or hydrogel membrane, consistent with our fibronectin-coated silicone platform evaluated here [18]. A limitation of our platform and many others in literature is a short mechanical stimulation period of 8 [13] to 72 h [43], similar to our stimulation time of 24 h [18]. This can be attributed to limited platform durability or sterility issues, as our platform's gearbox would overheat. This brief period of mechanical activation was sufficient in many studies to direct MSC alignment, proliferation, differentiation, or matrix production, consistent with our findings [18]. MSCs upregulated osteogenic, myogenic, or fibrotic markers and matrix factors after stimulation, consistent with our findings. Several studies investigated mechanical stimulation for much longer periods, up to 2- to 3-weeks of time, for a subset of hours per day [38, 44–47]. These long-term stimulations maintained MSC differentiation or matrix production but not alignment, potentially due to overgrowth of the MSC monolayer. It is important to note all table 3's references stimulated cultures by uniaxial tensile strain, whereas our soft robotic platform [18] offers multi-axial strain (angular bending and radial distention).

Despite the increased use of BigMACS in disease modelling and in cell or tissue biomanufacturing, the effect of mechanical forces on cell behaviour is non-deterministic and poorly understood. Lessons from microscale mechanobiology and macroscale biomechanics have taught us that mechanical forces create genetic, phenotypic, and functional changes in single cells which exhibit paracrine signals that, together with mechanical forces, easily propagate across a confluent tissue [11, 36, 51]. It is challenging to study these two mechanisms using BigMACS as the fabrication of big culture platforms can often

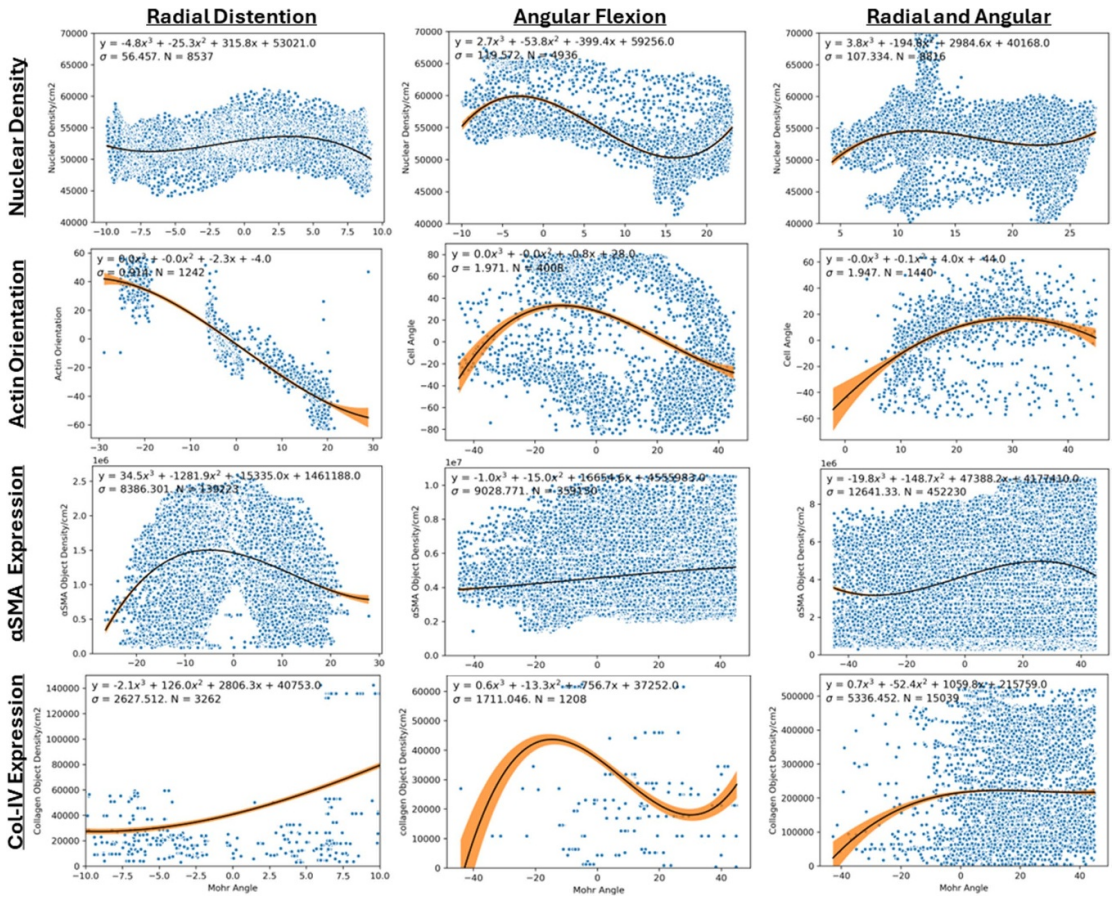

Figure 5. Impact of XY Mohr's stress angle on BigMACS cell behaviours. Scatterplots of *XY* Mohr's stress angle (*x*-axis) versus nuclear (DAPI stain) density, α-SMA stain density, and Col-IV stain density per cm^2 or average actin orientation, as calculated in a 50 μm radius around each detected stain. Third-order polynomials were fitted to the imaging data with 95% confidence intervals calculated. Regression statistical replicates were calculated as the number of stains detected per image (1201–451 749) and not imaging, experimental, or biological replicates.

create artefacts at the single-cell microscale [52], such as 3D printed layer lines [53], and because the application of physiological mechanical forces vary over large-scale cell culture chambers.

Our BigMACS framework, spatially correlating histological cell and protein quantitation to mechanical simulations, can help define mechanical tissue engineering design equations but has several limitations. One major limitation in this paper is experimental validation across replicate cultures, or different types of BigMACS cultures. This paper only evaluated correlations for one experimental cell culture replicate due to the large-format confocal images used. While our prior work indicates the outcomes from these wide-format images are consistent with regions of interest from four culture replicates [18], the variability of our correlations culture-to-culture is needed. Furthermore, we applied our framework to one type of BigMACS, and while we suggest it is useful to other systems such as tensile strain and media perfusion, these claims are untested.

Another limitation includes how our soft robotic system and its simulations do not model viscoelastic cues ubiquitous to biological systems. The soft robot bioreactor was injection-moulded with Platsil OO-20, a highly elastic silicone material. While this silicone can more feasibly recapitulate femoropopliteal artery distention with reasonable pressure, such an elastic silicone does not recapitulate the mechanics nor modulus of cardiovascular tissue. While we have shown other silicone elastomers (Sylgard or Solaris) better resemble vascular mechanics [54], silicones are limited in modelling viscoelastic mechanics.

Other specific limitations include our histology analysis' object detection, which considers each stain to be an individual entity instead of correlating it to a cell. For stains that resemble speckles, there can be tens to hundreds of speckles within each cell, resulting in overestimated regressions (in the case of αSMA in figures 4 and 5). We have previously done this by co-locating stains to individual nuclei within a given radius [55]. Finally, all imaged culture devices included injection-moulded microgrooves, and no smoothed-surface devices are analysed for comparison. While our prior work [18] indicates their impact is not statistically significant at a bulk scale, these microgrooves might create microscale confounding factors in addition to mechanical flexion.

Table 3. Effect of cyclic tensile strain on human mesenchymal stem cells (hMSCs). ALP—alkaline phosphatase; αSMA—α-smooth muscle actin; or BMP-2—bone morphogenetic protein 2; Cbfa1—core binding factor α1; FGF-2—fibroblast growth factor 2; IL1RN—interleukin-1 receptor antagonist; Runx2—Runt-related transcription factor 2; PDMS—Polydimethylsiloxane; SM22α—smooth muscle 22α; VEGF-A—vascular endothelial growth factor A.

Author, Year, [Reference]	Culture device	Actuation regime	Cell behaviour
Chen *et al*, 2008, [13]	Collagen-I coated scaffolds	3% cyclic tensile strain, 8 h.	Upregulation of osteoblastic markers, increased levels of ALP and Cbfa1. Cell alignment perpendicular to axis of strain.
		10% cyclic tensile strain, 48 h.	Increase in type collagen I, collagen III, and tenascin-C, indicating tenogenic differentiation. Cell alignment perpendicular to axis of strain.
Park *et al*, 2004, [48]	Elastin-coated membranes	10% cyclic tensile strain, 24 h, 1 Hz.	Transient increase in collagen I, α-actin, SM-22α, and β-actin. Cell alignment perpendicular to axis of strain.
		10% cyclic tensile strain, 3 d, 1 Hz.	SM-22α decreased by 25% after alignment. Cell alignment perpendicular to axis of strain.
	Collagen-coated membranes	10% cyclic tensile strain, 24 h, 1 Hz.	Transient increase in collagen I, α-actin, SM-22α, and β-actin. Cell alignment perpendicular to axis of strain.
		10% cyclic tensile strain, 24 h, 1 Hz.	10% cyclic tensile strain, 3 d, 1 Hz SM-22α decreased by 50% after alignment. Cell alignment perpendicular to axis of strain.
Khani *et al*, 2015, [49]	Collagen-coated PDMS.	5% cyclic tensile strain, 24 h, 1 Hz.	Strained cells without TGF-β1 significantly increased Young's Moduli and elevated levels of smooth muscle markers αSMA, h1-Calponin and SM 22 A. Strained hMSCs demonstrated increased myogenesis. Cell alignment perpendicular to axis of strain.
Koike *et al*, 2005, [50]	Collagen-I coated membranes	0.8% cyclic tensile strain, 48 h, 1 Hz.	Cbfa1/Runx2 increased. ALP activity increased.
		5% cyclic tensile strain, 48 h, 1 Hz.	Cell proliferation significantly increased. Cbfa1/Runx2 increased. Collagen I increased. Osteocalcin expression and ALP activity significantly decreased.
		10% cyclic tensile strain, 48 h, 1 Hz.	Cell proliferation significantly increased. Collagen I increased. Osteocalcin expression and ALP activity significantly decreased.
		15% cyclic tensile strain, 48 h, 1 Hz.	Cell proliferation significantly increased. Cbfal/Runx2 decreased. Collagen I Increased. Osteocalcin expression and ALP activity significantly decreased.
Jagodzinski *et al*, 2004, [43]	Silicone scaffold.	2% cyclic tensile strain, 6 h day^{-1} for 3 d, 1 Hz.	Increased ALP secretion and collagen III upregulation. Enhanced hMSC osteogenic commitment.
		8% cyclic tensile strain, 6 h day^{-1} for 3 d, 1 Hz.	Increased ALP secretion and collagen III upregulation. Collagen I and Cbfa1 upregulated. Enhanced hMSC osteogenic commitment.
Sumanasinghe *et al*, 2006, [44]	3D collagen matrix.	10% cyclic tensile strain, 4 h day^{-1} for 7 and 14 d, 1 Hz.	Increase in BMP-2 expression for both durations of strain.
		12% cyclic tensile strain, 4 h day^{-1} for 7 and 14 d, 1 Hz.	Increase in BMP-2 expression only in cells subjected to 14 d of strain.

(Continued.)

Table 3. (Continued.)

Author, Year, [Reference]	Culture device	Actuation regime	Cell behaviour
Charoenpanich *et al*, 2011, [45]	Collagen I gel sheet	10% cyclic tensile strain, 4 h day^{-1} for 14 d, 1 Hz.	Osteogenic differentiation, upregulation of IL1RN, FGF-2, VEGF-A.
Qiu *et al*, 2016, [46]	Collagen fibres	10% cyclic tensile strain, 12 h day^{-1} for 14 d, 1 Hz.	Collagen I, collagen III, tenascin-C, and fibroblastic transcription factor scleraxis upregulated. Tenogenic differentiation.
Yang *et al*, 2012, [47]	PEG hydrogels	10% cyclic tensile strain, 12 h day^{-1} for 14 d, 1 Hz.	Upregulated collagen III and upregulated tenascin-C. No cell alignment observed.
Altman *et al*, 2002, [38]	Collagen or silk fibre matrices	6.7% cyclic translation for 21 d, 0.0167 Hz	Increased bone marrow MSC cell density by up to two-fold as compared to static.

5. Conclusion

In this study we developed a computational modelling and quantitative histology framework to identify what local mechanical force is required for desired local and bulk changes in cell behaviour. Identifying these relationships will help us formulate fundamental mechanical design equations for gradient tissue modelling and biomanufacturing. Due to microscale artefacts ubiquitous in BigMACS fabrication or surface processes, we developed our centimetre-scale FEA simulation to have microscale resolution. For each of the 2-to-10 thousand cells imaged in our BigMACS culture chamber, our FEA simulation would average hundreds of local mechanical stresses required for simulation convergence.

Our innovative FEA simulation and quantitative histology framework derived new relationships on how principal stress magnitude and direction appear to pattern MSC behaviour. Specifically, smooth muscle (SMC) differentiation by MSCs was found to have a positive correlation with local areas of high stress in all mechanically conditioned BigMACS, suggesting that soft robotic bioreactors are a promising tool to controllably design and engineer gradient smooth muscle tissue, including zones of potent MSCs and zones of differentiated SMCs. We found that cell orientation is inversely proportional to mechanical principal stress direction but only for radial BigMACS and not more complex actuation modes. In contrast, we found that increasing mechanical stress magnitude could not be used to locally pattern MSC nuclear density and Col-IV deposition; indicating these are cell behaviours that rapidly propagate across culture space and would be challenging to spatially confine with BigMACS. The local principal stress direction did not play any significant role on local cell orientation or other behaviours, suggesting some cell behaviours are dependent on regional mechanics and are challenging to locally control and pattern at a single-cell scale. The application of our framework to our soft robotic BigMACS bioreactor is limited by the analysis of only one culture replicate of each mechanical actuation condition. Biological and technical replicates must be performed in future studies to validate any proposed mechanobiology design equations.

To our knowledge, this is the first FEA simulation able to predict subcellular mechanical forces in the presence of microroughness often found in dynamic tissue engineered cell cultures; and this is the first framework that applies these microscale FEA simulation results to single-cell quantitative histology across large, mechanically-patterned tissues (10 000's of cells; centimetres of tissue). Our new FEA mechanical simulation and quantitative histology framework are a powerful tool for investigating how BigMACS can be designed or engineered to apply mechanical forces which control microscale gradients of mechanical forces able to locally or regionally pattern cells and tissues for disease modelling and biomanufacturing. This framework opens new doors to formulate the fundamental design equations of mechanically-patterned tissue biomanufacturing.

Data availability statement

All data that support the findings of this study are included within the article (and any supplementary files).

Acknowledgments

This work was supported by a GOstralia!-GOzealand! GmbH Scholarship to SS, a Bionics Queensland Grand Challenge Award to SS, CAF, MCA, a British Heart Foundation Centre of Research Excellence Award (RE/18/4/34215) and a Delft Technology Fellowship to SP, a Strategic Partnership Award for Research Collaboration of the Chinese University of

Hong Kong (4930640) to HFC and MCA, Australian Research Council funding to YCT and MCA (FT150100398, DP230100721, DE220100757), and an Advance Queensland fellowship (AQIRF1312018) to MCA.

Conflict of interest

The authors declare that they have no known competing financial interests or personal relationships that could have appeared to influence the work reported in this paper. DFF consults to the local Ansys distributors which gives him access to Ansys technical staff as needed.

ORCID iDs

Sabrina Schoenborn https://orcid.org/0000-0002-9240-893X
Mingyang Yuan https://orcid.org/0009-0000-5419-9826
Cody A Fell https://orcid.org/0000-0002-1509-5116
David F Fletcher https://orcid.org/0000-0003-2221-4192
Selene Priola https://orcid.org/0000-0003-4368-3940
Hon Fai Chan https://orcid.org/0000-0003-0573-1251
Mia Woodruff https://orcid.org/0000-0002-4909-5288
Zhiyong Li https://orcid.org/0000-0002-6814-9165
Yi-Chin Toh https://orcid.org/0000-0002-4105-4852
Mark C Allenby https://orcid.org/0000-0003-0423-4560

References

[1] Vining K H and Mooney D J 2017 Mechanical forces direct stem cell behaviour in development and regeneration *Nat. Rev. Mol. Cell Biol.* **18** 728–42
[2] Sun M *et al* 2018 Effects of matrix stiffness on the morphology, adhesion, proliferation and osteogenic differentiation of mesenchymal stem cells *Int. J. Med. Sci.* **15** 257
[3] Kim S, Uroz M, Bays J L and Chen C S 2021 Harnessing mechanobiology for tissue engineering *Dev. Cell* **56** 180–91
[4] Katoh K 2023 Effects of mechanical stress on endothelial cells *in situ* and *in vitro Int. J. Mol. Sci.* **24** 16518
[5] Zhang X, Zhang S and Wang T 2022 How the mechanical microenvironment of stem cell growth affects their differentiation: a review *Stem Cell Res. Ther.* **13** 415
[6] Huang X, Huang Z, Gao W, Gao W, He R, Li Y, Crawford R, Zhou Y, Xiao L and Xiao Y 2022 Current advances in 3D dynamic cell culture systems *Gels* **8** 829
[7] Uto K, Tsui J H, DeForest C A and Kim D-H 2017 Dynamically tunable cell culture platforms for tissue engineering and mechanobiology *Prog. Polym. Sci.* **65** 53–82
[8] Gaspar D A, Gomide V and Monteiro F J 2012 The role of perfusion bioreactors in bone tissue engineering *Biomatter* **2** 167–75
[9] Somers S M, Spector A A, DiGirolamo D J and Grayson W L 2017 Biophysical stimulation for engineering functional skeletal muscle *Tissue Eng. B* **23** 362–72
[10] Paek J, Song J W, Ban E, Morimitsu Y, Osuji C O, Shenoy V B and Huh D D 2021 Soft robotic constrictor for *in vitro* modeling of dynamic tissue compression *Sci. Rep.* **11** 16478
[11] Sun Y, Wan B, Wang R, Zhang B, Luo P, Wang D, Nie J-J, Chen D and Wu X 2022 Mechanical stimulation on mesenchymal stem cells and surrounding microenvironments in bone regeneration: regulations and applications *Front. Cell Dev. Biol.* **10** 808303
[12] Steward A J and Kelly D J 2015 Mechanical regulation of mesenchymal stem cell differentiation *J. Anat.* **227** 717–31
[13] Chen Y-J, Huang C-H, Lee I-C, Lee Y-T, Chen M-H and Young T-H 2008 Effects of cyclic mechanical stretching on the mRNA expression of tendon/ligament-related and osteoblast-specific genes in human mesenchymal stem cells *Connect. Tissue Res.* **49** 7–14
[14] Torii R, Velliou R-I, Hodgson D and Mudera V 2018 Modelling multi-scale cell–tissue interaction of tissue-engineered muscle constructs *J. Tissue Eng.* **9** 2041731418787141
[15] Chen C S, Tan J and Tien J 2004 Mechanotransduction at cell-matrix and cell-cell contacts *Annu. Rev. Biomed. Eng.* **6** 275–302
[16] Hou Y, Yu L, Xie W, Camacho L C, Zhang M, Chu Z, Wei Q and Haag R 2019 Surface roughness and substrate stiffness synergize to drive cellular mechanoresponse *Nano Lett.* **20** 748–57
[17] Mok S, Al Habyan S, Ledoux C, Lee W, MacDonald K N, McCaffrey L and Moraes C 2020 Mapping cellular-scale internal mechanics in 3D tissues with thermally responsive hydrogel probes *Nat. Commun.* **11** 4757
[18] Fell C, Brooks-Richards T L, Woodruff M A and Allenby M C 2022 Soft pneumatic actuators for mimicking multi-axial femoropopliteal artery mechanobiology *Biofabrication* **14** 035005
[19] Lévesque L, Loy C, Lainé A, Drouin B, Chevallier P and Mantovani D 2017 Incrementing the frequency of dynamic strain on SMC-cellularised collagen-based scaffolds affects extracellular matrix remodeling and mechanical properties *ACS Biomater. Sci. Eng.* **4** 3759–67
[20] Rabbani M, Tafazzoli-Shadpour M, Shokrgozar M A, Janmaleki M and Teymoori M 2017 Cyclic stretch effects on adipose-derived stem cell stiffness, morphology and smooth muscle cell gene expression *Tissue Eng. Regen. Med.* **14** 279–86
[21] Walters B, Uynuk-Ool T, Rothdiener M, Palm J, Hart M L, Stegemann J P and Rolauffs B 2017 Engineering the geometrical shape of mesenchymal stromal cells through defined cyclic stretch regimens *Sci. Rep.* **7** 6640
[22] Kreutzer J, Viehrig M, Pölönen R-P, Zhao F, Ojala M, Aalto-Setälä K and Kallio P 2020 Pneumatic unidirectional cell stretching device for mechanobiological studies of cardiomyocytes *Biomech. Model. Mechanobiol.* **19** 291–303
[23] Han P, Guo T, Jayasree A, Gomez G A, Gulati K and Ivanovski S 2023 Tunable nano-engineered anisotropic surface for enhanced mechanotransduction and soft-tissue integration *Nano Res.* **16** 7293–303
[24] Vartanian S M and Conte M S 2015 Surgical intervention for peripheral arterial disease *Circ. Res.* **116** 1614–28
[25] Shu J and Santulli G 2018 Update on peripheral artery disease: epidemiology and evidence-based facts *Atherosclerosis* **275** 379–81
[26] Hackett R M 2016 *Hyperelasticity Primer* 2nd edn (Springer)
[27] Ogden R 1973 Large deformation isotropic elasticity—on the correlation of theory and experiment for incompressible rubberlike solids *Rubber Chem. Technol.* **46** 398–416
[28] Moseley P, Florez J M, Sonar H A, Agarwal G, Curtin W and Paik J 2016 Modeling, design, and development of soft pneumatic actuators with finite element method *Adv. Eng. Mater.* **18** 978–88

[29] The University of Queensland Research Computing Centre 2024 *Bunya supercomputer* Brisbane, Queensland, Australia (https://doi.org/10.48610/wf6c-qy55)
[30] Barsanescu P D and Comanici A M 2017 von Mises hypothesis revised *Acta Mech.* **228** 433–46
[31] Lee J Y, Ryu H R and Park Y T 2014 Finite element implementation for computer-aided education of structural mechanics: Mohr's circle and its practical use *Comput. Appl. Eng. Educ.* **22** 494–508
[32] Mohr O 1882 Über die Darstellung des Spannungszustandes und des Deformationszustandes eines Körperelementes und über die Anwendung derselben in der Festigkeitslehre *Der Civilingenieur* **28** 113–56
[33] Rezakhaniha R *et al* 2012 Experimental investigation of collagen waviness and orientation in the arterial adventitia using confocal laser scanning microscopy *Biomech. Model. Mechanobiol.* **11** 461–73
[34] Allenby M C, Misener R, Panoskaltsis N and Mantalaris A 2017 A quantitative three-dimensional image analysis tool for maximal acquisition of spatial heterogeneity data *Tissue Eng. C* **23** 108–17
[35] Relaix F *et al* 2021 Perspectives on skeletal muscle stem cells *Nat. Commun.* **12** 692
[36] Tao J, Choudhury M I, Maity D, Kim T, Sun S X and Fan C-M 2023 Mechanical compression creates a quiescent muscle stem cell niche *Commun. Biol.* **6** 43
[37] Sillat T, Saat R, Pöllänen R, Hukkanen M, Takagi M and Konttinen Y T 2012 Basement membrane collagen type IV expression by human mesenchymal stem cells during adipogenic differentiation *J. Cell Mol. Med.* **16** 1485–95
[38] Altman G H, Lu H H, Horan R L, Calabro T, Ryder D, Kaplan D L, Stark P, Martin I, Richmond J C and Vunjak-Novakovic G 2002 Advanced bioreactor with controlled application of multi-dimensional strain for tissue engineering *J. Biomech. Eng.* **124** 742–9
[39] Cao W, Lin W, Cai H, Chen Y, Man Y, Liang J, Wang Q, Sun Y, Fan Y and Zhang X 2019 Dynamic mechanical loading facilitated chondrogenic differentiation of rabbit BMSCs in collagen scaffolds *Regen. Biomater.* **6** 99–106
[40] Wei F *et al* 2022 Changes in interstitial fluid flow, mass transport and the bone cell response in microgravity and normogravity *Bone Res.* **10** 65
[41] Tsata V and Beis D 2020 In full force. Mechanotransduction and morphogenesis during homeostasis and tissue regeneration *J. Cardiovascular Dev. Dis.* **7** 40
[42] Wong T-Y, Chang S-N, Jhong R-C, Tseng C-J, Sun G-C and Cheng P-W 2019 Closer to nature through dynamic culture systems *Cells* **8** 942
[43] Jagodzinski M, Drescher M, Zeichen J, Hankemeier S, Krettek C, Bosch U and van Griensven M 2004 Effects of cyclic longitudinal mechanical strain and dexamethasone on osteogenic differentiation of human bone marrow stromal cells *Eur. Cell Mater.* **7** 41
[44] Sumanasinghe R D, Bernacki S H and Loboa E G 2006 Osteogenic differentiation of human mesenchymal stem cells in collagen matrices: effect of uniaxial cyclic tensile strain on bone morphogenetic protein (BMP-2) mRNA expression *Tissue Eng.* **12** 3459–65
[45] Charoenpanich A, Wall M E, Tucker C J, Andrews D M K, Lalush D S and Loboa E G 2011 Microarray analysis of human adipose-derived stem cells in three-dimensional collagen culture: osteogenesis inhibits bone morphogenic protein and Wnt signaling pathways, and cyclic tensile strain causes upregulation of proinflammatory cytokine regulators and angiogenic factors *Tissue Eng. A* **17** 2615–27
[46] Qiu Y, Lei J, Koob T J and Temenoff J S 2016 Cyclic tension promotes fibroblastic differentiation of human MSCs cultured on collagen-fibre scaffolds *J Tissue Eng. Regen. Med.* **10** 989–99
[47] Yang P J, Levenston M E and Temenoff J S 2012 Modulation of mesenchymal stem cell shape in enzyme-sensitive hydrogels is decoupled from upregulation of fibroblast markers under cyclic tension *Tissue Eng. A* **18** 2365–75
[48] Park J S, Chu J S F, Cheng C, Chen F, Chen D and Li S 2004 Differential effects of equiaxial and uniaxial strain on mesenchymal stem cells *Biotechnol. Bioeng.* **88** 359–68
[49] Khani M-M, Tafazzoli-Shadpour M, Goli-Malekabadi Z and Haghighipour N 2015 Mechanical characterization of human mesenchymal stem cells subjected to cyclic uniaxial strain and TGF-β1 *J. Mech. Behav. Biomed. Mater.* **43** 18–25
[50] Koike M, Shimokawa H, Kanno Z, Ohya K and Soma K 2005 Effects of mechanical strain on proliferation and differentiation of bone marrow stromal cell line ST2 *J. Bone Miner. Metab.* **23** 219–25
[51] Argentati C, Morena F, Tortorella I, Bazzucchi M, Porcellati S, Emiliani C and Martino S 2019 Insight into mechanobiology: how stem cells feel mechanical forces and orchestrate biological functions *Int. J. Mol. Sci.* **20** 5337
[52] Madrid-Sánchez A, Duerr F, Nie Y, Thienpont H and Ottevaere H 2022 Fabrication of large-scale scaffolds with microscale features using light sheet stereolithography *Int. J. Bioprint.* **9** 650
[53] Lerman M J, Lembong J, Gillen G and Fisher J P 2018 3D printing in cell culture systems and medical applications *Appl. Phys. Rev.* **5** 041109
[54] Schoenborn S, Lorenz T, Kuo K, Fletcher D F, Woodruff M A, Pirola S and Allenby M C 2023 Fluid-structure interactions of peripheral arteries using a coupled in silico and *in vitro* approach *Comput. Biol. Med.* **165** 107474
[55] Allenby M C, Panoskaltsis N, Tahlawi A, Dos Santos S B and Mantalaris A 2019 Dynamic human erythropoiesis in a three-dimensional perfusion bone marrow biomimicry *Biomaterials* **188** 24–37